

## Non-uniform temperature distribution of the main reflector of a large radio telescope under solar radiation

Shan-Xiang Wei<sup>1,2,3</sup>, De-Qing Kong<sup>1,3\*</sup> and Qi-Ming Wang<sup>2,3\*</sup>

<sup>1</sup> Key Laboratory of Lunar and Deep Space Exploration, National Astronomical Observatories, Chinese Academy of Sciences, Beijing 100101, China; [kdq@bao.ac.cn](mailto:kdq@bao.ac.cn), [qmwang@bao.ac.cn](mailto:qmwang@bao.ac.cn)

<sup>2</sup> Key Laboratory of FAST, National Astronomical Observatories, Chinese Academy of Sciences, Beijing 100101, China

<sup>3</sup> University of Chinese Academy of Sciences, Beijing 100049, China

Received 2021 July 19; accepted 2021 September 7

**Abstract** The non-uniform temperature distribution of the main reflector of a large radio telescope may cause serious deformation of the main reflector, which will dramatically reduce the aperture efficiency of a radio telescope. To study the non-uniform temperature field of the main reflector of a large radio telescope, numerical calculations including thermal environment factors, the coefficients on convection and radiation, and the shadow boundary of the main reflector are first discussed. In addition, the shadow coverage and the non-uniform temperature field of the main reflector of a 70-m radio telescope under solar radiation are simulated by finite element analysis. The simulation results show that the temperature distribution of the main reflector under solar radiation is very uneven, and the maximum of the root mean square temperature is 12.3°C. To verify the simulation results, an optical camera and a thermal imaging camera are used to measure the shadow coverage and the non-uniform temperature distribution of the main reflector on a clear day. At the same time, some temperature sensors are used to measure the temperature at some points close to the main reflector on the backup structure. It has been verified that the simulation and measurement results of the shadow coverage on the main reflector are in good agreement, and the cosine similarity between the simulation and the measurement is above 90%. Despite the inevitable thermal imaging errors caused by large viewing angles, the simulated temperature field is similar to the measured temperature distribution of the main reflector to a large extent. The temperature trend measured at the test points on the backup structure close to the main reflector without direct solar radiation is consistent with the simulated temperature trend of the corresponding points on the main reflector with the solar radiation. It is credible to calculate the temperature field of the main reflector through the finite element method. This work can provide valuable references for studying the thermal deformation and the surface accuracy of the main reflector of a large radio telescope.

**Key words:** large radio telescope — finite element analysis — solar radiation — shadow coverage — temperature distribution

### 1 INTRODUCTION

Large radio telescopes are widely employed in deep space exploration and astronomical research. A typical large-scale and fully-steerable radio telescope, the Wuqing 70-m radio telescope, is shown in Figure 1. The structure of the radio telescope antenna consists of five parts: the subreflector and quadripod, the main reflector and backup structure, the elevation cradle, the alidade structure, and the azimuth rail. The main reflector of a radio telescope, supported by the backup structure, is served

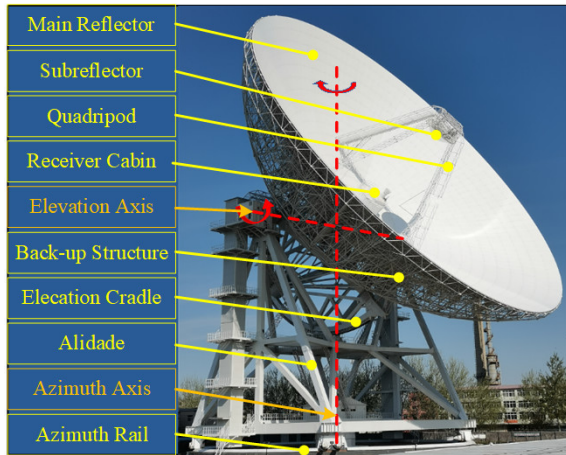
as a device to gather electromagnetic waves from the universe. It can point in any direction by moving around the vertical azimuth axis and the horizontal elevation axis (Baars & Kärcher 2018). Generally, radio telescopes are expected to have good reflector accuracy to receive radio waves more effectively (Ye et al. 2020). Due to the effects of gravity, non-uniform temperature, and wind disturbance, the deformation of the main reflector of a large radio telescope is inevitable. The gravity-induced deformation of the main reflector is repeatable, which can be compensated appropriately through some predictable adjustments (Bergstrand et al. 2019). However, the non-

---

\* Corresponding author

**Table 1** Material Properties of Aluminum Alloy Plane of Main Reflector

Density ( $\text{kg m}^{-3}$ )	Specific Heat ( $\text{J kg}^{-1} \text{K}^{-1}$ )	Thermal Conductivity ( $\text{W m}^{-1} \text{K}^{-1}$ )	Thermal Expansion ( $10^{-6} \text{K}^{-1}$ )	Absorptivity	Emissivity
2700	960	203	23.21	0.6	0.8

**Fig. 1** The Wuqing 70-m radio telescope.

uniform temperature field and the random wind field are always time-varying, which will cause a dynamic deformation of the main reflector (Greve & Bremer 2010; Ranka et al. 2016). The dynamic deformation of the main reflector may seriously affect the aperture efficiency of a radio telescope. Therefore, studying the non-uniform temperature field of the main reflector of a large radio telescope is very significant for improving the performance of radio telescopes.

The thermal design and thermal behavior of radio telescopes have been studied internationally through finite element (FE) analysis and experimental tests, such as the thermal design of the quadripod and backup structure of the IRAM 30-m telescope (Greve et al. 2005), the thermal behavior of the yoke, main reflector and backup structure of the ALMA 12-m prototype antenna (Greve & Mangum 2008), the thermal analysis of the alidade of the Sardinia 64-m telescope (Pisanu et al. 2014), and so on. In China, the related studies have also been carried out in several radio telescopes in recent years, including the thermal analysis of the main active reflector and supporting structure of the FAST 500-m radio telescope (Song & Wang 2016; Wang et al. 2017), the thermal behavior of the alidade and backup structure of the Tianma 65-m radio telescope (Fu et al. 2016; Dong et al. 2018), the thermal effects of the alidade of the Miyun 50-m radio telescope (Kong et al. 2019) and the Wuqing 70-m radio telescope (Wei et al. 2021). In particular, several experimental studies on the temperature field of the main reflector are conducted in some small testing radio telescopes, as a 3-m radio telescope in Harbin Institute of Technology (Chen et al. 2016) and a 7.3-m radio telescope in Xidian

University (Lian et al. 2020). In theory, two methods, the contact temperature sensor measurement and the non-contact thermal imaging measurement, can be used to measure the temperature field of the main reflector of a large radio telescope. However, an abundance of the contact temperature sensors arranged in the main reflector may affect the surface accuracy. So far, most of the research on the temperature field of the main reflector of large radio telescopes has remained at the stage of numerical analysis.

The Wuqing 70-m radio telescope is the largest fully steerable radio telescope in China. The influence of the non-uniform temperature field of the main reflector (hereinafter referred to as the main reflector) of the Wuqing 70-m radio telescope on the reflector accuracy cannot be ignored. In order to obtain the credible temperature field of the main reflector under solar radiation, corresponding numerical and experimental studies are carried out. First, the theoretical derivation on the thermal environment factors, the convection and emissivity coefficients, and the shadow boundary of the main reflector is completed. Then, the shadow coverage and temperature distribution of the main reflector are simulated through FE analysis. At the same time, the shadow coverage and temperature distribution of the main reflector are measured with an optical camera and a thermal imaging camera on a clear day. In addition, some temperature sensors are installed to measure the temperature at certain points on the backup structure close to the main reflector. Finally, the results of the simulation and experiment are analyzed and compared.

## 2 THEORETICAL STUDY FOR THE MAJOR FACTORS AFFECTING HEAT TRANSFER OF MAIN REFLECTOR

Heat transfer occurs through heat conduction, convection, and radiation, the numerical derivation of which have been introduced in a document (Greve & Bremer 2010). The basic theories of the three types of heat exchange are perfect in thermodynamics and will not be covered here. The heat transfer process of the main reflector is affected by some complex factors, including the structural material properties, the solar radiation intensity on earth, the temperatures for sky and ground, the convective coefficient, the radiation angle coefficient, the structural shadow coverage, and so on.

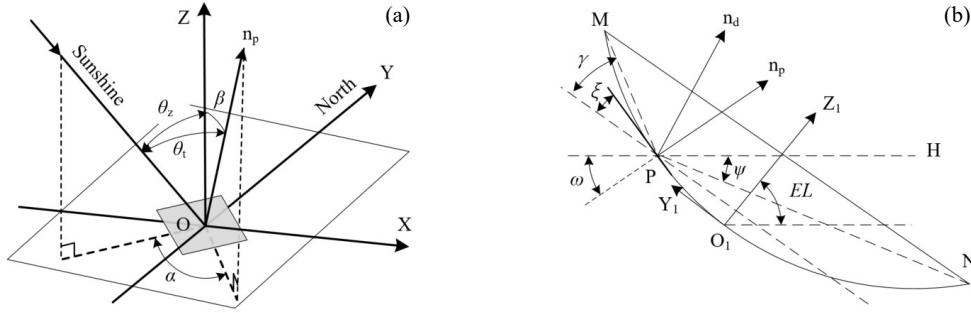


Fig. 2 Sketch of solar radiation on the main reflector: (a) direct radiation, (b) sky and ground radiation.

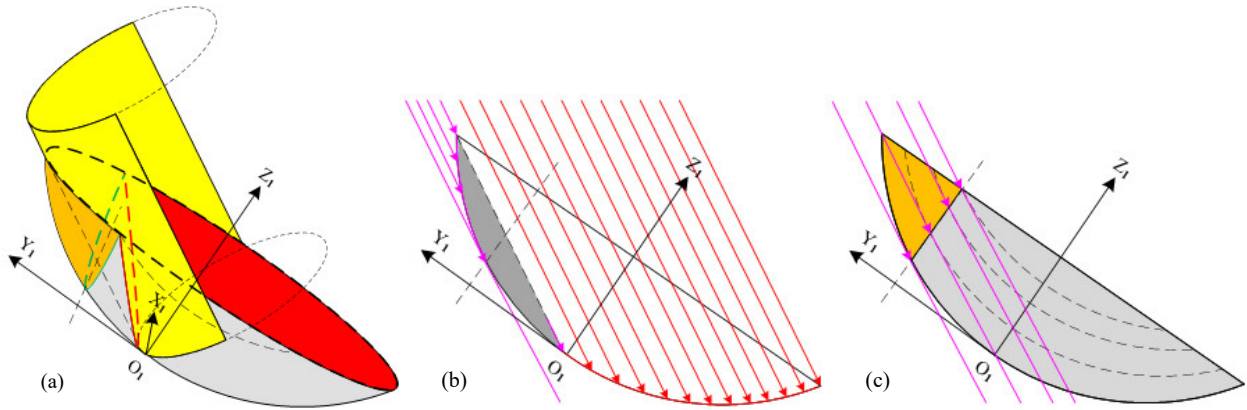


Fig. 3 Sketch of shadow boundary on the main reflector: (a) three-dimensional view, (b) sectional view along the  $Y_1Z_1$  plane, (c) front view.

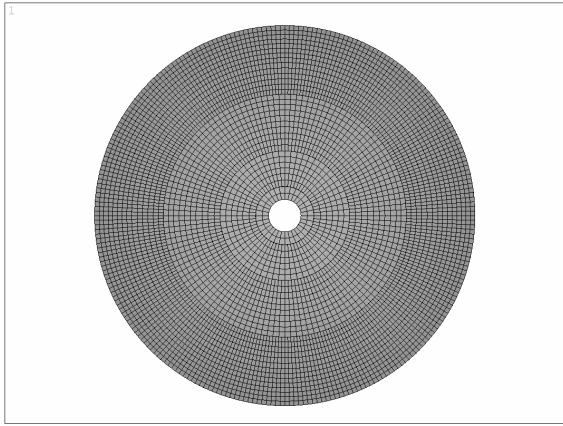


Fig. 4 FE thermal-analysis model of the main reflector.

### 2.1 Thermal Environment of the Wuqing 70-m Radio Telescope

The thermal environment is one of the main factors affecting the temperature of a large radio telescope. The 70-meter radio telescope site in Wuqing has a flat terrain with an altitude close to sea level. Some environmental parameters on the site, including the ambient air temperature, the wind speed, the atmospheric pressure, and the humidity, have been measured with

a weather station. Based on the measured ambient air temperature, the sky temperature  $T_s$  can be calculated as (Greve & Bremer 2010)

$$T_s(t) = 0.0553T_a^{1.5}(t), \quad (1)$$

and the ground temperature  $T_g$  can be calculated as (Greve & Bremer 2010)

$$T_g(t) = T_a(t) + \Delta T_g(t), \quad (2)$$

where  $T_a$  is the ambient air temperature,  $\Delta T_g$  is a temperature variation amplitude and it can be approximately expressed as  $10 \sin[(t - 8)\pi/12]$  (Qian et al. 2016). Here,  $t$  is the local time.

The total solar radiation radiated to an object on earth consists of direct solar radiation, diffuse solar radiation, and reflecting solar radiation. According to the ASHRAE model for a clear sky, the direct solar radiation intensity  $G_b$  is expressed as (Abouhashish 2017)

$$G_b = A \cdot e^{(-P/P_o)(B/\sin \beta_s)} \cdot C_N, \quad (3)$$

the diffuse solar radiation intensity  $G_d$  is expressed as (Abouhashish 2017)

$$G_d = C \cdot G_b, \quad (4)$$

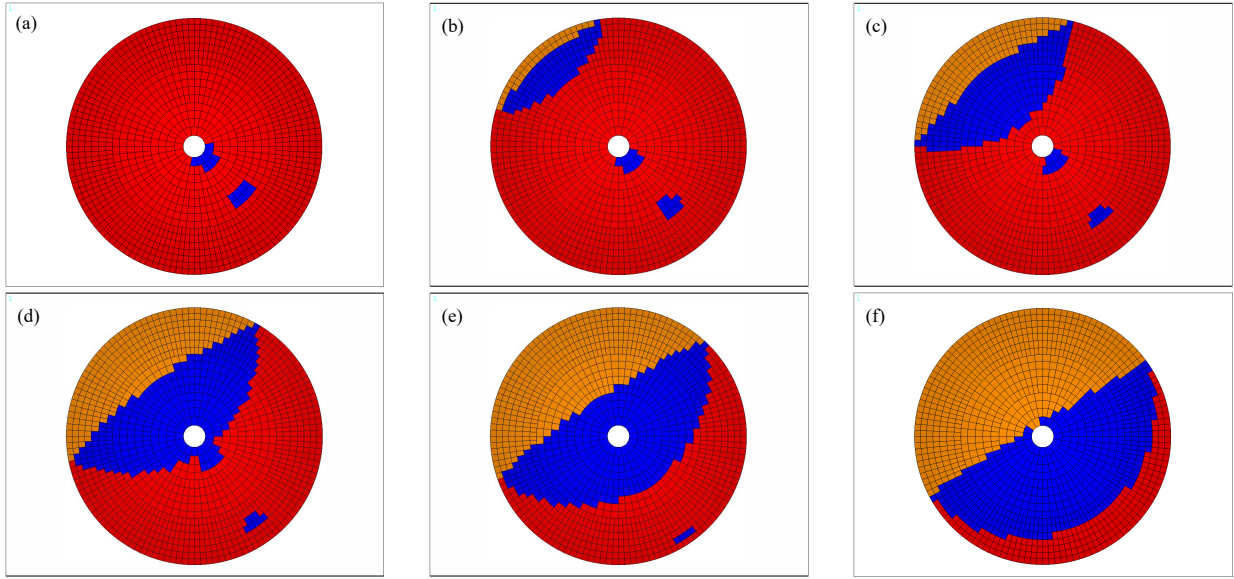


**Fig. 5** Simulated shadows of the main reflector on 2021 April 4 (Beijing time): (a)11:00, (b)11:30, (c)12:00, (d)12:30, (e)13:00, (f)13:30.

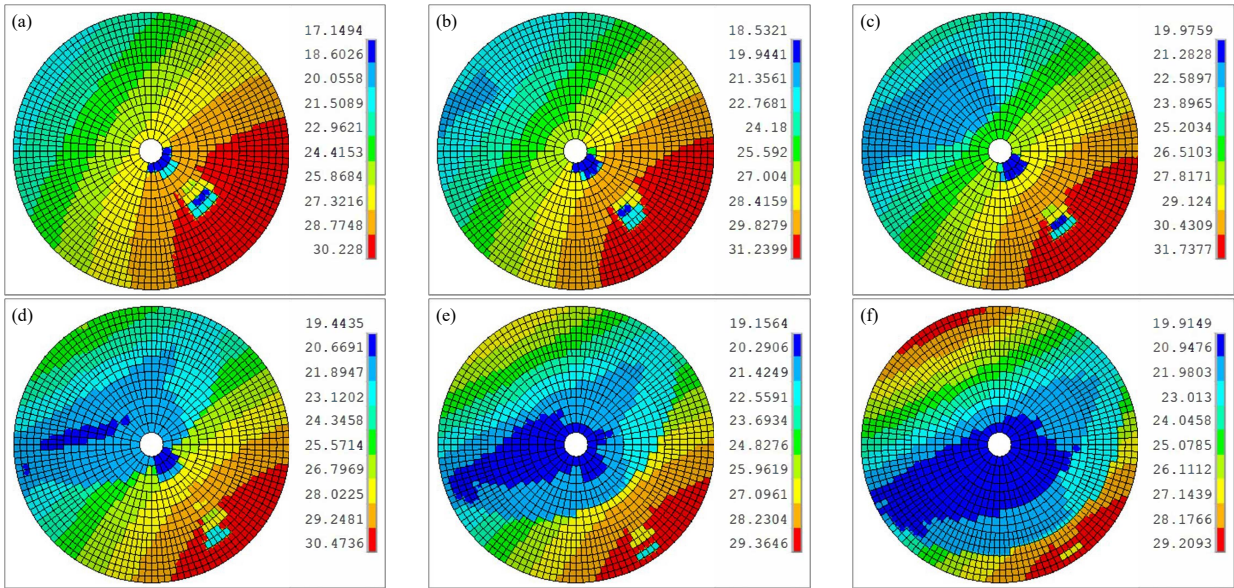


**Fig. 6** Simulated temperature contours of the main reflector on 2021 April 4 (Beijing time): (a)11:00, (b)11:30, (c)12:00, (d)12:30, (e)13:00, (f)13:30.

and the reflecting solar radiation intensity  $G_r$  is expressed as (Abouhashish 2017)

$$G_r = \tau \cdot (G_b \cdot \sin \beta_s + G_d), \quad (5)$$

where  $A$  is the solar radiation outside the atmosphere and its value can be calculated as  $(1162.12 + 77.0323 * \cos 360n/365)$ ,  $B$  is the atmospheric extinction coefficient and its value can be calculated as  $(0.171076 - 0.0348944 * \cos 360n/365)$ ,  $C$  is the diffuse radiation factor and its value can be calculated as  $(0.0897334 - 0.0412439 * \cos 360n/365)$ ,  $n$  is the number of days in one year,  $P$  is the pressure of the local atmosphere, ( $P_o = 101325Pa$ )

is the pressure of a standard atmosphere,  $C_N$  is clearness factor,  $\beta_s$  is solar altitude, and  $\tau$  is the surface reflectance of the site.

Therefore, the total solar radiation  $G_t$  absorbed into a single reflecting plane of the main reflector can be calculated as (Abouhashish 2017)

$$G_t = \epsilon \cdot (G_b \cdot \varphi_b + G_d \cdot \varphi_s + G_r \cdot \varphi_g), \quad (6)$$

where  $\epsilon$  is the solar absorptance of a reflecting plane,  $\varphi_b$  is the angle coefficient for direct solar radiation,  $\varphi_s$  is the angle coefficient for sky radiation,  $\varphi_g$  is the angle coefficient for ground radiation. To be specific, these

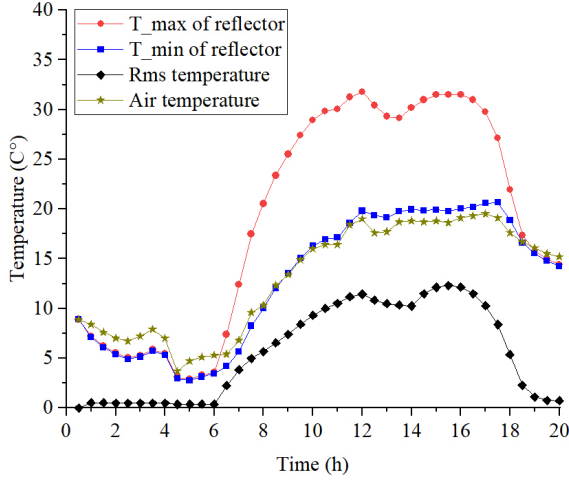


**Fig. 7** The maximum, minimum and root mean square of the simulated temperature of the main reflector.

radiation angle coefficients will be introduced in the next subsection.

## 2.2 Coefficients for Convection and Radiation

Convective heat transfer coefficient and radiation angle coefficient are the major factors affecting the uniformity of the temperature distribution on the main reflector. To lessen the effects of the wind speed on the uniformity of the temperature distribution on the main reflector, the actual environment conditions on a windless sunny day are selected as the boundary conditions of the FE thermal-analysis of the main reflector.

Air convection can be treated as the surface loads to act on the meshed elements of the main reflector directly. The convective heat transfer coefficient  $h_c$  can be given as (Greve & Bremer 2010)

$$h_c = 0.664R_e^{1/2} \cdot P_r^{1/3} \cdot k/L, \quad (7)$$

where the Reynolds Number  $R_e = vL\rho(z)/\mu$ , the Prandtl Number  $P_r = \mu/\rho(z)\eta$ , the air thermal diffusivity  $\eta = k/\rho(z)\lambda$ ,  $v$  is the wind speed,  $\rho(z)$  is the air density related to altitude,  $\mu$  is the air absolute viscosity,  $\lambda$  is the air heat capacity at constant pressure,  $L$  is the length of the object in the direction of the fluid, and  $k$  is the air thermal conductivity.

Solar radiation and long-wave radiation can be treated as the equivalent heat generation rate to act on the meshed elements of the main reflector. As Figure 2(a) shows,  $\theta_t$  is the incident angle of the solar beam on a reflecting plane,  $\theta_z$  is the zenith angle of the Sun,  $\beta$  is the tilt angle of a reflecting plane, and  $\alpha$  is the azimuth difference between a reflecting plane and the solar beam. For a single reflecting plane of the main reflector exposed to solar radiation, the angle coefficient  $\varphi_b$  for direct solar radiation can be

calculated as (Greve & Bremer 2010)

$$\varphi_b = \cos \theta_t = \cos \theta_z \cos \beta + \sin \theta_z \cos \alpha \sin \beta. \quad (8)$$

As is shown in Figure 2(b), the local coordinate system  $O_1X_1Y_1Z_1$  is established,  $\mathbf{n}_p$  is the normal vector at point P,  $\mathbf{n}_d$  is an arbitrary vector within radiation  $\angle MPH$ ,  $\gamma$  is the angle between  $\overline{PM}$  and the line parallel to  $Y_1$  axis,  $\psi$  is the angle between  $\overline{PN}$  and the line parallel to  $Y_1$  axis,  $\xi$  is the angle between the tangent at point P and the line parallel to  $Y_1$  axis,  $\omega$  is the angle between  $\mathbf{n}_p$  and the horizontal line  $\overline{PH}$ , and  $EL$  is the elevation angle of a radio telescope. According to the geometric relationship in Figure 2(b), the angle coefficient  $\varphi_{sce}$  of the main reflector concave for sky radiation can be expressed as (Chen et al. 2016)

$$\varphi_{sce} = [\cos(\xi - \gamma) - \sin(\xi - EL)]/2, \quad (9)$$

the angle coefficient  $\varphi_{gce}$  of the main reflector concave for ground radiation can be expressed as (Chen et al. 2016)

$$\varphi_{gce} = [\cos(\xi + \psi) + \sin(\xi - EL)]/2, \quad (10)$$

the angle coefficient  $\varphi_{scx}$  of the main reflector convex for sky radiation can be expressed as (Chen et al. 2016)

$$\varphi_{scx} = (1 - \sin \omega)/2, \quad (11)$$

and the angle coefficient  $\varphi_{gcx}$  of the main reflector convex for ground radiation can be expressed as (Chen et al. 2016)

$$\varphi_{gcx} = (1 + \sin \omega)/2. \quad (12)$$

## 2.3 Shadow Boundary of Main Reflector

The shadow coverage of the main reflector is mainly affected by the main reflector itself, subreflector, and receiver cabin. The shadow coverage of the main reflector itself is more complicated, which will be discussed in detail here. The main reflector is a paraboloid and the focal diameter ratio  $F/D$  is 0.3. The projection of the aperture edge of the main reflector on the normal plane of sunlight is an ellipse. The ellipse is stretched into an elliptical cylinder along the direction of sunlight, as shown in Figure 3(a). For the concave of the main reflector, the shadow boundary of the main reflector is the intersection curve of the paraboloid and the elliptical cylinder. According to the geometric relationship in Figure 3(b), the equation of the intersection curve in the coordinate system  $O_1X_1Y_1Z_1$  can be expressed as

$$\begin{cases} (x^2 + y^2)/4F - z = 0, \\ \quad \text{where } x \in [0, 35] \text{ and } y \in [0, 35] \\ x^2 + (y - z \tan \theta)^2 - 35 = 0, \\ \quad \text{where } 0 \leq y - z \tan \theta \leq 35 \end{cases}, \quad (13)$$

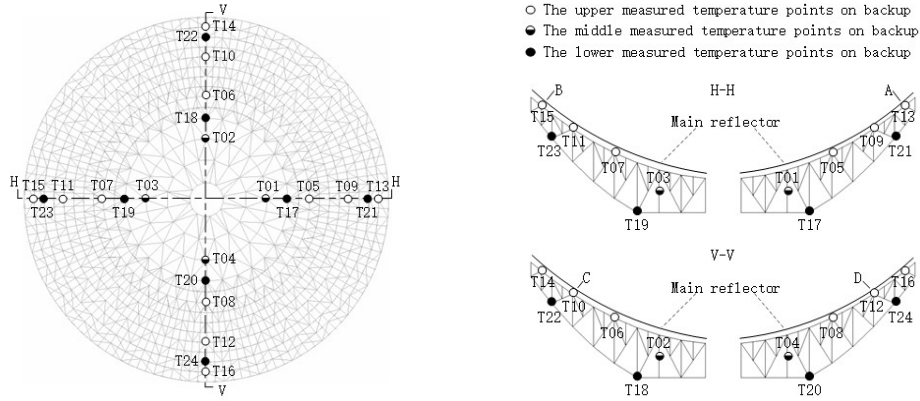


**Fig. 8** Distribution of temperature sensors on the backup structure: (a) the top view, (b) the section views on H-H plane and V-V plane.

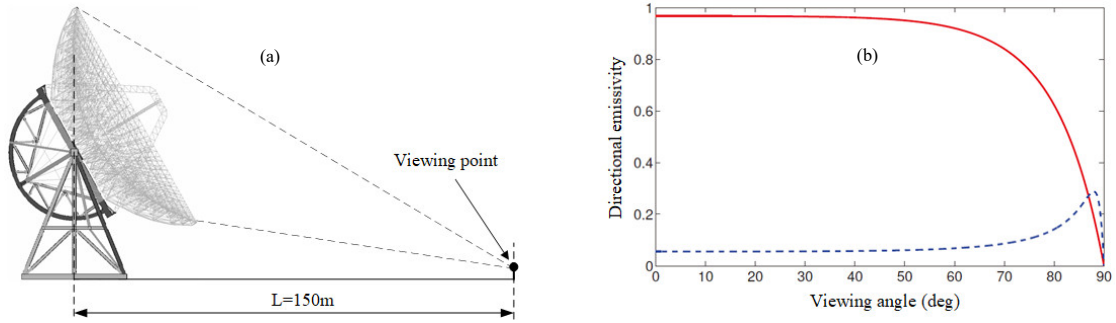


**Fig. 9** Viewing point and emissivity characteristics: (a) viewing point of the thermal imaging camera relative to the 70-m radio telescope, (b) exemplary comparison of the general emissivity characteristics of dielectrics (*solid line*) and metals (*dashed line*) (Zeise et al. 2015).

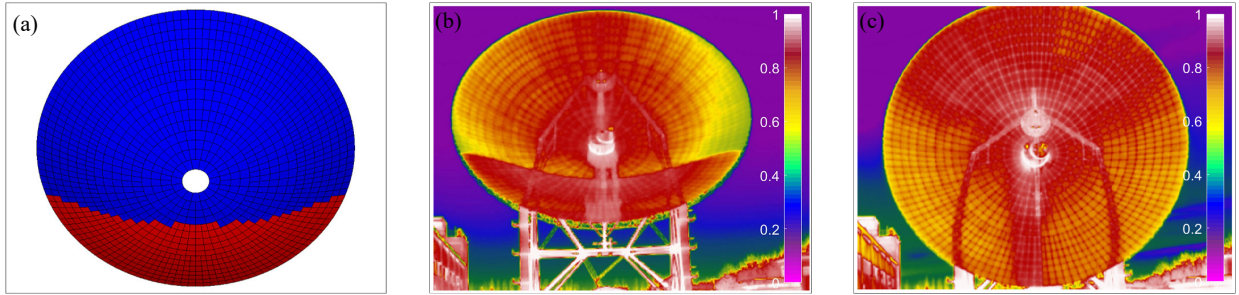


**Fig. 10** Emissivity characteristics of different viewing angle: (a) the reflecting planes of the main reflector with a viewing angle of more than  $60^\circ$ , (b) the measured relative temperature distributions of the main reflector at the elevation of  $30^\circ$ , (c) the measured relative temperature distributions of the main reflector at the elevation of  $7^\circ$ .

where  $F$  is the focal length of the main reflector,  $\theta$  is the incident angle of the solar beam on the aperture plane of the main reflector. According to the geometric relationship in Figure 3(c), the curves of the paraboloid on different sections paralleling to the  $Y_1Z_1$  plane are homologous parabolas, the first derivatives with respect to  $y$  of which can be expressed as  $\partial z/\partial y = y/2F$ . Given the sunlight paralleling to the  $Y_1Z_1$  plane, all the tangent points of sunlight on the convex of the paraboloid at a certain time will be on one plane paralleling to the  $X_1Z_1$  plane. Therefore, the shadow boundary of the convex of the main

reflector is the intersection curve of the paraboloid and the plane containing all the tangent points of sunlight. The curve equation can be expressed as

$$\begin{cases} z = (x^2 + y^2) / 4F \\ y = 2F \cot \theta \end{cases}, \quad (14)$$

where  $F$  and  $\theta$  is same as Equation (13). Similarly, the shadows of the subreflector and receiver cabin can also be calculated, which will not be discussed here.

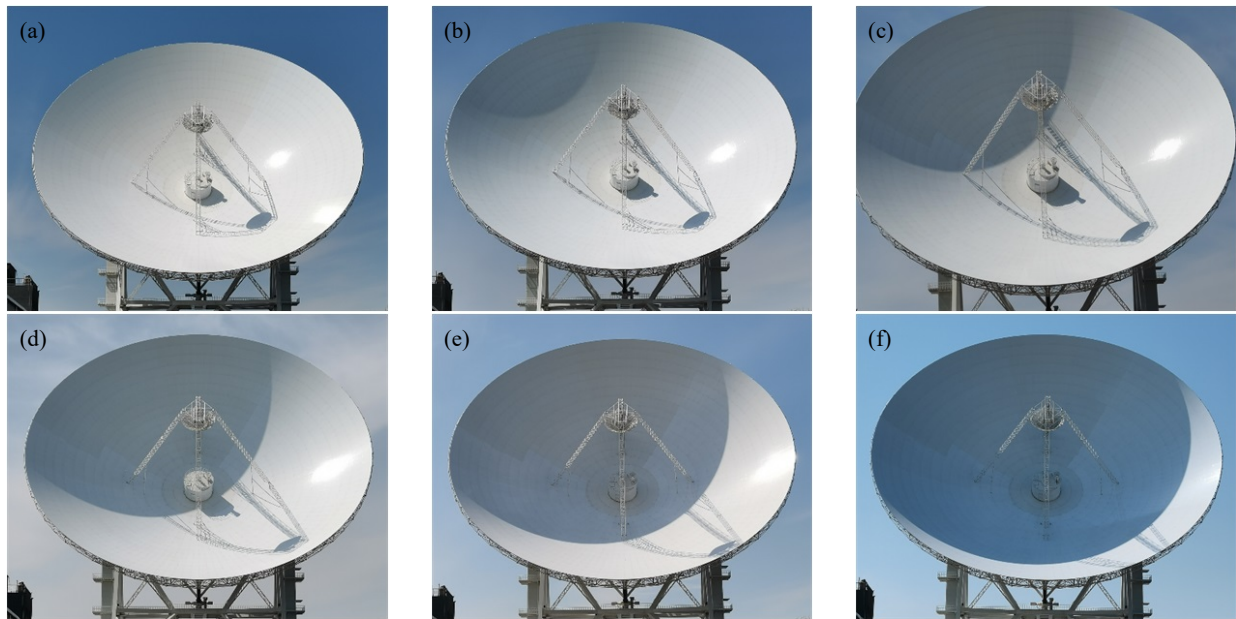


**Fig. 11** Recorded shadows of the main reflector on 2021 April 4 (Beijing time): (a)11:00, (b)11:30, (c)12:00, (d)12:30, (e)13:00, (f)13:30.

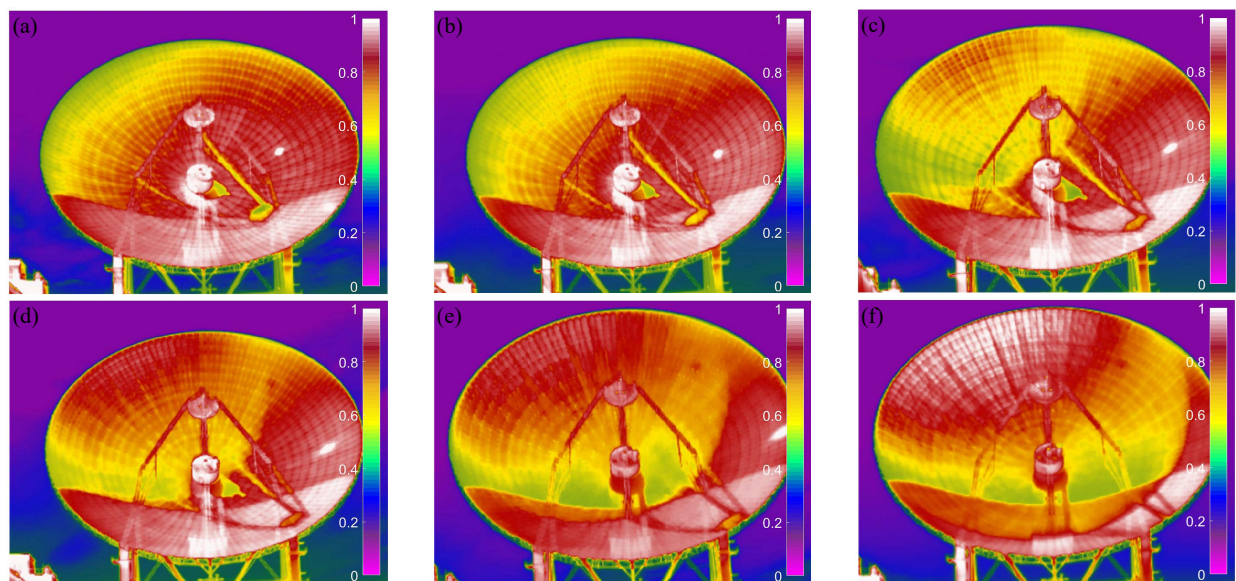


**Fig. 12** Measured temperature contours of the main reflector on 2021 April 4 (Beijing time): (a)11:00, (b)11:30, (c)12:00, (d)12:30, (e)13:00, (f)13:30.

### 3 SIMULATIONS ON SHADOW COVERAGE AND TEMPERATURE DISTRIBUTION OF MAIN REFLECTOR

#### 3.1 FE Model of Main Reflector

The shadow coverage and temperature distribution of the main reflector under solar radiation can be simulated by FE software. The FE thermal-analysis model of the main reflector is shown in Figure 4. The element type of the main reflector is shell131, which is a 3-D layered shell element having in-plane and through-thickness thermal conduction

capability. The material property of the aluminum alloy plane of the main reflector is presented in Table 1 (Liu et al. 2014).

#### 3.2 Simulation on Shadow Coverage of Main Reflector

The shadow coverage of the main reflector under solar radiation is related to the telescope's working condition and the Sun's position. The shadow coverage of the main reflector can be marked with color in a three-dimension

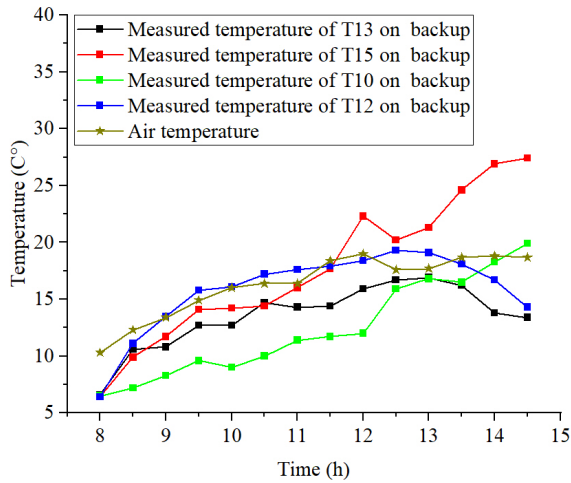


**Fig. 13** The measured temperatures of the test points of T13, T15, T12 and T10 on backup structure.

model. Figure 5(a)–(f) are the simulated shadows of the main reflector under solar radiation from 11:00 to 13:30 on 2021 April 4 (Beijing time), when the Wuqing 70-m radio telescope was kept at the position of the elevation angle  $30^\circ$  and the azimuth angle  $90^\circ$ .

### 3.3 Simulation on Temperature Distribution of Main Reflector

To ensure the reliability of the thermal analysis, the boundary conditions of the FE thermal analysis model of the main reflector should be kept consistent with the actual environmental conditions as much as possible. The simulated temperature contours of the main reflector under solar radiation from 11:00 to 13:30 on 2021 April 4 (Beijing time) are presented in Figure 6, when the Wuqing 70-m radio telescope was kept at the position of the elevation angle  $30^\circ$  and the azimuth angle  $90^\circ$ . The trends of the maximum, minimum, and root mean square (RMS) of the simulated temperature on the main reflector on 2021 April 4 (Beijing time) are shown in Figure 7 and the maximum of the temperature RMS is  $12.3^\circ\text{C}$ .

## 4 EXPERIMENTS ON SHADOW COVERAGE AND TEMPERATURE DISTRIBUTION OF MAIN REFLECTOR

### 4.1 Experiment Description

To verify the simulation results, the actual shadow coverage and temperature distribution of the main reflector were measured with an optical camera and a thermal imaging camera. At the same time, the temperature of some special points of the backup structure is monitored through contact temperature sensors, where the test points of T13, T15, T12, and T10 on the backup structure are

respectively close to the points of A, B, C, and D on the main reflector, as shown in Figure 8.

The date of the experiment is 2021 April 4 (Beijing time), when the Wuqing 70-m radio telescope was maintained at the elevation angle of  $30^\circ$  and the azimuth angle of  $90^\circ$ . Due to the limited field of view of the thermal imaging camera, the measurement error increases as the distance increases. Therefore, a proper viewing point should be selected to obtain a complete and high-quality infrared image of the temperature distribution of the main reflector. Figure 9(a) shows the viewing point of the thermal imaging camera relative to the azimuth axis of the Wuqing 70-m radio telescope. In addition, when the viewing angle of the partial reflecting planes exceeds the effective measurement range of the thermal reflector, the emissivity of these reflecting planes will increase sharply, and the measured relative temperature distribution of the main reflector is not accurate. Figure 9(b) is an exemplary comparison of the general emissivity characteristics of dielectrics and metals. It indicates that the emissivity of metal surfaces has a constantly low value at viewing angles from  $0^\circ$  to  $60^\circ$ , and then grows to a maximum just before reaching a minimum at  $90^\circ$  (Zeise et al. 2015).

In order to verify the above emissivity characteristics of the aluminum alloy planes of the main reflector, from the determined viewing point, the reflecting planes with a viewing angle of more than  $60^\circ$  are marked with red, as shown in Figure 10(a). In addition, when the Wuqing 70-m radio telescope was maintained at the elevation angle of  $30^\circ$  (at 21:00) and  $7^\circ$  (at 20:00) on 2021 April 3 (Beijing time), the relative temperature distribution of the main reflector was respectively measured from the determined viewing point, as Figure 10(b) and Figure 10(c). The results show that the emissivity characteristics of the aluminum alloy planes of the main reflector are consistent with the emissivity characteristics of the metal described in Figure 9(b).

### 4.2 Experiment Results

The measurement results of the shadow coverage of the main reflector from 11:00 to 13:30 on 2021 April 4 (Beijing time) are shown in Figure 11.

Due to the effects of the atmospheric absorption and the viewing angle, the absolute temperature of the main reflector measured by the thermal imaging camera is unreliable. Fortunately, the relative temperature distribution of the main reflector measured by the thermal imaging camera is also valuable. It can verify the simulation results of the non-uniform temperature distribution of the main reflector. The final relative temperature distribution of the main reflector, measured by a thermal imaging camera on 2021 April 4 (Beijing time), is shown in Figure 12. The measured temperature of the test points of T13, T15, T12,

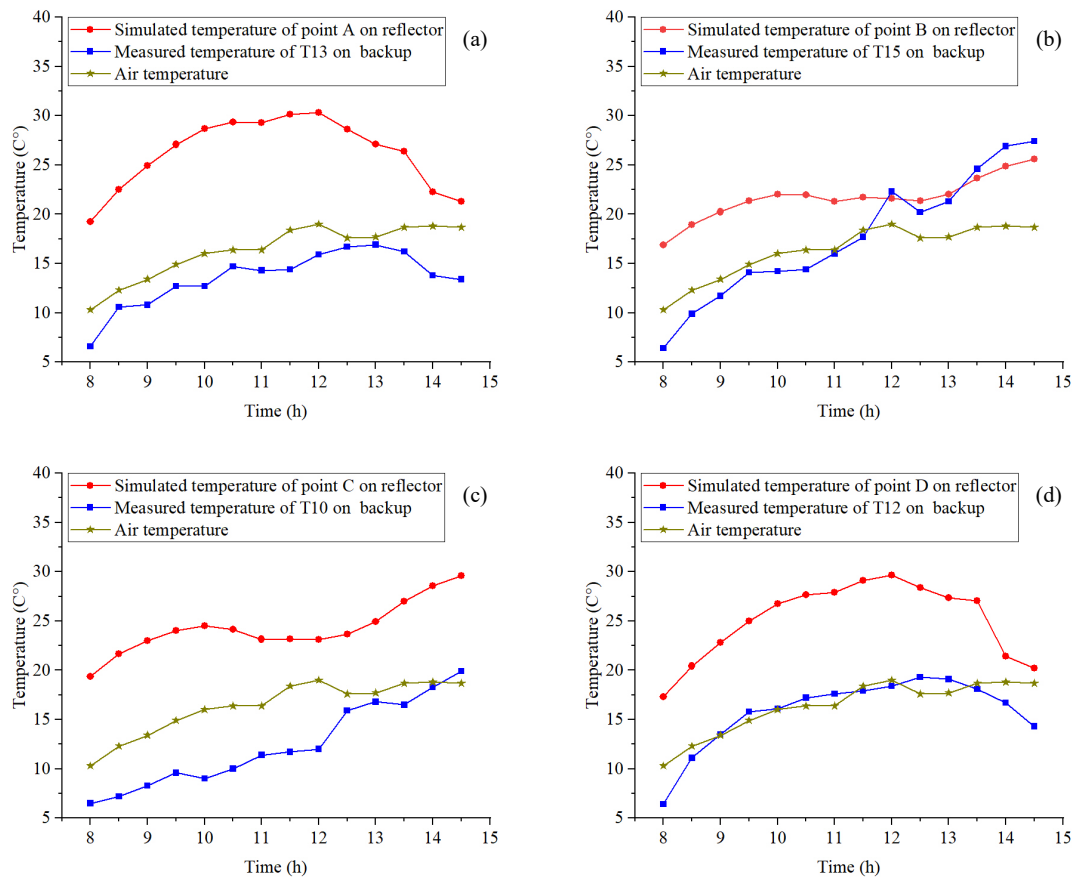


**Fig. 14** The comparison between the measured temperature of the test points of T13, T15, T10 and T12 on backup structure and the simulated temperature of the points of A, B, C, and D on main reflector: (a) between T13 and A, (b) between T15 and B, (c) between T10 and C, (d) between T12 and D.

and T10 on the backup structure is shown in Figure 13. The measurement results show that the temperature distribution of the main reflector under solar radiation is closely relative to the shadow coverage of the main reflector.

### 4.3 Discussion on the Results of Simulation and Experiment

Comparing Figure 5 and Figure 11, it is not difficult to find that the simulation and measurement results of the shadow coverage of the main reflector are in good agreement. After removing the background and extracting shadow features, the cosine similarities between the simulated shadow and the measured shadow of the main reflector at different times on 2021 April 4 all exceed 90%. In addition, for the relative temperature distribution of the main reflector, the simulation results in Figure 6 are also consistent with the measurement results in Figure 12 to a large extent. Finally, the comparison between the measured temperature of the test points of T13, T15, T10, and T12 on the backup structure and the simulated temperature of the points of A, B, C, and D on the main reflector is presented in Figure 14. The comparison results show that the temperature trend

measured at the test points on the backup structure close to the main reflector without direct solar radiation is in good agreement with the simulated temperature trend of the corresponding points on the main reflector with solar radiation, as Figure 14(a) and (d). The temperature trend measured at the test points on the backup structure close to the main reflector with direct solar radiation is getting closer to or even exceeding the simulated temperature trend of the corresponding points on the main reflector with solar radiation, such as Figure 14(b) and (c).

## 5 CONCLUSIONS

The main reflector of the Wuqing 70-m radio telescope is taken as the research object in this paper, a credible temperature field of which is acquired by numerical and experimental studies. Based on the results of simulation and measurement of the shadow coverage and temperature distribution of the main reflector, the conclusion can be drawn as follows.

(1) The non-uniform temperature distribution of the main reflector under solar radiation is very obvious. According to the numerical research, the maximum of the temperature RMS of the main reflector is up to 12.3°C.

(2) The calculation of the shadow boundary on the main reflector is reliable. The simulated shadow of the main reflector is in good agreement with the measured shadow and the cosine similarity of the two is above 90%.

(3) It is credible to calculate the temperature field of the main reflector through FE thermal analysis. Despite the inevitable thermal imaging errors caused by large viewing angles, the simulation and measurement results of the relative temperature distribution of the main reflector are in agreement to a large extent.

(4) The temperature distribution of the main reflector has great effects on the temperature field of the backup structure. The temperature trend measured at the test points on the backup structure close to the main reflector without direct solar radiation is consistent with the simulated temperature trend of the corresponding points on the main reflector with solar radiation.

**Acknowledgements** This work was funded by the Astronomical Joint Fund of National Natural Science Foundation of China and Chinese Academy of Sciences (U1831114) and the National Natural Science Foundation of China (11673040 and 11803053).

## References

- Abouhashish, M. 2017, in American Institute of Physics Conference Series, 1850, Solarpaces 2016: International Conference on Concentrating Solar Power and Chemical Energy Systems, 140001
- Baars, J. W. M., & Kärcher, H. J. 2018, Radio Telescope Reflectors, 447 (Springer International Publishing AG)
- Bergstrand, S., Herbertsson, M., Rieck, C., et al. 2019, Journal of Geodesy, 93, 669
- Chen, D. S., Qian, H. L., Wang, H. J., et al. 2016, Applied Thermal Engineering, 111, 1130
- Dong, J., Fu, L., Liu, Q., et al. 2018, Experimental Astronomy, 45, 397
- Fu, L., Ling, Q. B., Geng, X. G., et al. 2016, in Society of Photo-Optical Instrumentation Engineers (SPIE) Conference Series, 9912, Advances in Optical and Mechanical Technologies for Telescopes and Instrumentation II, eds. R. Navarro, & J. H. Burge, 99124J
- Greve, A., & Bremer, M. 2010, Thermal Design and Thermal Behaviour of Radio Telescopes and their Enclosures, 364 (Springer)
- Greve, A., Bremer, M., Penalver, J., et al. 2005, IEEE Transactions on Antennas and Propagation, 53, 851
- Greve, A., & Mangum, J. 2008, IEEE Antennas and Propagation Magazine, 50, 66
- Kong, D. Q., Jiang, Z. Y., Zhang, H. B., et al. 2019, Scientia Sinica Technologica (in Chinese), 49, 1331
- Lian, P. Y., Wang, C. S., Xu, Q., et al. 2020, IET Microwaves, Antennas & Propagation, 14, 1635
- Liu, H. B., Chen, Z. H., Han, Q. H., et al. 2014, Thin-Walled Structures, 85, 15
- Pisanu, T., Buffa, F., Poppi, S., et al. 2014, in Society of Photo-Optical Instrumentation Engineers (SPIE) Conference Series, 9145, Ground-based and Airborne Telescopes V, eds. L. M. Stepp, R. Gilmozzi, & H. J. Hall, 91454R
- Qian, H. L., Chen, D. S., Fan, F., et al. 2016, International Journal of Steel Structures, 16, 383
- Ranka, T., Garcia-Sanz, M., Symmes, A., et al. 2016, Journal of Astronomical Telescopes, Instruments, and Systems, 2, 014001
- Song, L. Q., & Wang, Q. M. 2016, in Society of Photo-Optical Instrumentation Engineers (SPIE) Conference Series, 9682, 8th International Symposium on Advanced Optical Manufacturing and Testing Technologies: Large Mirrors and Telescopes, eds. M. K. Cho, & B. Fan, 968204
- Wang, Q. M., Zhu, M., Wang, Q. M., et al. 2017, in Advances in Engineering Research, 102, Second International Conference on Mechanics, Materials and Structural Engineering (ICMMSE 2017), eds. D. K. Kim, J. W. Hu, & J. K. Ahn, 201
- Wei, S.-X., Kong, D.-Q., & Wang, Q.-M. 2021, RAA (Research in Astronomy and Astrophysics), 21, 137
- Ye, Q., Huang, J., Jin, H., et al. 2020, Optics and Lasers in Engineering, 134, 106249
- Zeise, B., Kleinschmidt, S. P., & Wagner, B. 2015, in 2015 IEEE International Symposium on Safety, Security, and Rescue Robotics (SSRR), 1